Examination of sulfate resistance of nano-alumina added ordinary Portland cement paste, focusing on the two different crystallinity of nano-aluminas

Juan Yu[1], Sungwon Sim[1], Haemin Song[1], Dohoon Kim[1], Kyungcheol Jang[1], Dongho Jeon[1], Seung Cho[1,2] and Jae Eun Oh[1]*

Abstract

This study examined the influence of the crystallinity of added nano-alumina on the sulfate resistance of ordinary Portland cement (OPC) paste. Two crystalline types of nano-aluminas (α-and γ-phase) were incorporated in cement pastes, which were exposed to sulfate solution. In the results, both paste samples having α- and γ-phase aluminas had accelerated compressive strength loss and increased length expansion compared to the sample without alumina addition. In particular, the rapidly decreased dynamic elastic modulus of the nano-alumina added samples postulates the greatly increased internal stress likely by the increased formation of volume expansive reaction products, such as ettringite, which was supported by the XRD and TG results. The greater ettringite formation in the nano-alumina added samples was likely due to reactive AH_3 ($=Al(OH)_3$) gel formation as the higher consumption degree of portlandite in the alumina added samples indirectly indicates the active AH_3 gel formation, resulting in additional ettringite formation from the reaction of AH_3 with Na_2SO_4 solution. A further degree of sulfate attack was observed in the γ-alumina added sample for the long-term Na_2SO_4 exposure (180 days) mainly due to the greater degree of gypsum formation inducing more internal expansive stress compared to the α-alumina added sample.

Keywords Nano-alumina, Ordinary Portland cement, Degree of crystallinity, Alumina dissolution, Sulfate attack, α- and γ-alumina

*Correspondence:
Jae Eun Oh
ohjaeeun@unist.ac.kr
[1] School of Urban and Environmental Engineering, Ulsan National Institute of Science and Technology (UNIST), UNIST-gil 50, Ulju-gun, Ulsan 44919, Republic of Korea
[2] Division for Structural Engineering and Civil Engineering Informatics, Department of Civil Engineering, Stellenbosch University, Stellenbosch 7600, South Africa

1 Introduction

The pulverization of micro-sized spherical materials (e.g., SiO_2, TiO_2, Al_2O_3, or Fe_2O_3) into nano-scale materials has continued to gain research interest in the construction material field as it introduces several benefits when incorporated, such as morphological rearrangement of cementitious materials on the nanometer scale (Mukhopadhyay, 2011). Nanometer-sized alumina (Al_2O_3) (hereafter referred to as nano-alumina) is one of them, and the nano-alumina addition can improve the mechanical properties and durability of cementitious materials, as reported by other studies (Chen et al., 2018; Farzadnia et al., 2013; Li et al., 2017; Maagi et al., 2019; Mohseni et al., 2019; Shahrajabian

& Behfarnia, 2018; Zhan et al., 2019). In general, alumina is categorized into two classes: (1) α-alumina: crystalline alumina with lower surface areas, (2) η- or γ-alumina: poorly crystalline alumina having high surface areas (Acikgoz et al., 2018; Maciver et al., 1963; Newsome et al., 1960).

The influence of nano-alumina incorporation on cementitious binders depends on the crystallinity of nano-alumina. Shao and Zhou et al. (Shao et al., 2019; Zhou et al., 2019) investigated the influence of nano-sized γ-alumina on OPC at short- and long-term curing periods and found that the incorporated nano-alumina was dissolved in alkaline conditions (pH = ~ 13), resulting in increasing the quantity of aluminum-bearing hydration products such as ettringite, monosulfate [$Ca_4Al_2O_6(SO_4) \cdot 14H_2O$], and monocarboaluminate [$Ca_4Al_2O_7(CO_2) \cdot 11H_2O$]. Another study showed that the amorphous nano-alumina accelerated the silicate and aluminate phases reactions in OPC and reduced macropores, resulting in early strength improvement (Zhan et al., 2019). In the case of CaO-activated GGBFS binder, it was found that the higher dissolution rate of amorphous nano-alumina (i.e., γ-alumina) increased the amount of hydration products formation, such as calcium silicate hydrate (C-S-H) and ettringite [$Ca_6Al(SO_4)_3(OH)_{12} \cdot 26H_2O$], which improved the compressive strength (Yu et al., 2021).

In addition, the sulfuric content in the nano-alumina added cementitious binders affected the type of reaction hydrates (Shao et al., 2019; Yu et al., 2021; Zhou et al., 2019). In CaO-activated GGBFS binders, for instance, the formation of monosulfate was dominant, and the leftover of dissolved alumina turned into amorphous AH_3 gel when enough sulfur was not supplied (Yu et al., 2021). However, in high sulfur concentration conditions, the AH_3 gel reacted with the sulfur and calcium from calcium oxide resulting in a high amount of ettringite formation (Yu et al., 2021). Similarly, in OPC binders, the dissolved alumina accelerated gypsum consumption which led to a rapid ettringite formation at an early age (Zhou et al., 2019). In the long-term period, the monosulfate formation was dominated instead of ettringite formation, and the dissolved alumina also increased the monocarboaluminate content which was possibly formed by atmospheric CO_2 (Shao et al., 2019).

It is widely known that the chemical characteristics of amorphous nano-alumina may enhance the mechanical properties of cementitious binders (Shao et al., 2019; Yu et al., 2021; Zhan et al., 2019; Zhou et al., 2019). However, it may raise potential durability issues, particularly the sulfate attack; the residual AH_3 gel conversion to ettringite can occur when sulfur is ingressed from the outside, such as in a sewer or seawater environment.

The late ettringite formation can cause severe volume expansion in the cementitious binders, resulting in crack propagation and disintegration. (Dyer 2014; Mehta and Monteiro, 2014).

On the other hand, if the binders become denser through pore refinement by nano-alumina incorporation, the sulfur penetration in the binder matrix could be inhibited, which leads to a reduction in the expansive crack propagation (Zhan et al., 2019). In a similar case, nano-silica played a role in preventing sulfur leaching by making the binder denser and enhancing the anti-cracking effect (Huang et al., 2020; Qudoos et al., 2019; Xie et al., 2019a). Gopalakrishnan et al. (Gopalakrishnan & Jeyalakshmi, 2020) evaluated the sulfate resistance of nano-alumina added OPC mortar and found that the improved sulfate resistance of the mortars by nano-alumina addition. However, this study could not correctly validate the influence of nano-alumina incorporation in pure OPC binders exposed to sulfur sources primarily because of the presence of other pozzolanic materials, i.e., fly ash, in that OPC mortar, which can be a sulfate resistance improving factor (Dyer 2014; Gopalakrishnan & Jeyalakshmi, 2020; Xie et al., 2019b).

From this point of view, in this study, the following two aspects of nano-alumina must be addressed to encourage the application of nano-alumina in practice: (1) the variation of the dissolution rate of nano-alumina due to the different crystallinity reacting with ingressing sulfate causing internal volume expansion; (2) the prospect of cementitious matrix densification to disrupt sulfur penetration. This study employed two different crystalline types of nano-aluminas, i.e., α- and γ-aluminas, on OPC paste. Various mechanical tests (compressive strength test, visual inspection, length change measurement, longitudinal dynamic elastic moduli of cement paste), and chemical analyses [powder X-ray diffraction (XRD), and thermogravimetry (TG) with derivative of thermogravimetry (DTG)] were conducted to discuss the effect of nano-alumina inclusion towards the sulfate attack resistance.

2 Experimental Procedure
2.1 Raw Materials
OPC was obtained from Sampyo Cement Co., Ltd., Seoul, Republic of Korea. Nano-aluminas (α and γ types of nano-aluminas) were sourced from the Lumi-M Co. (Seoul, Republic of Korea).

The raw OPC was analyzed with the X-ray fluorescence (XRF) using an S8 Tiger wavelength dispersive XRF spectrometer (Bruker, Billerica, MA, USA). The oxide chemical composition of the raw OPC is presented in Table 1, which shows the dominance of CaO and SiO_2 (i.e., the sum of CaO and SiO_2 was 81.68

Yu *et al. Int J Concr Struct Mater*   (2023) 17:32

Page 3 of 11

Table 1 Oxide chemical composition of raw ordinary Portland cement (wt%)

CaO	SiO$_2$	Al$_2$O$_3$	MgO	SO$_3$	Fe$_2$O$_3$	K$_2$O	TiO$_2$	Na$_2$O	P$_2$O$_5$	Others
63.51	18.17	4.43	4.01	3.83	3.44	1.54	0.29	0.18	0.16	0.44

Fig. 1 XRD pattern of raw ordinary Portland cement
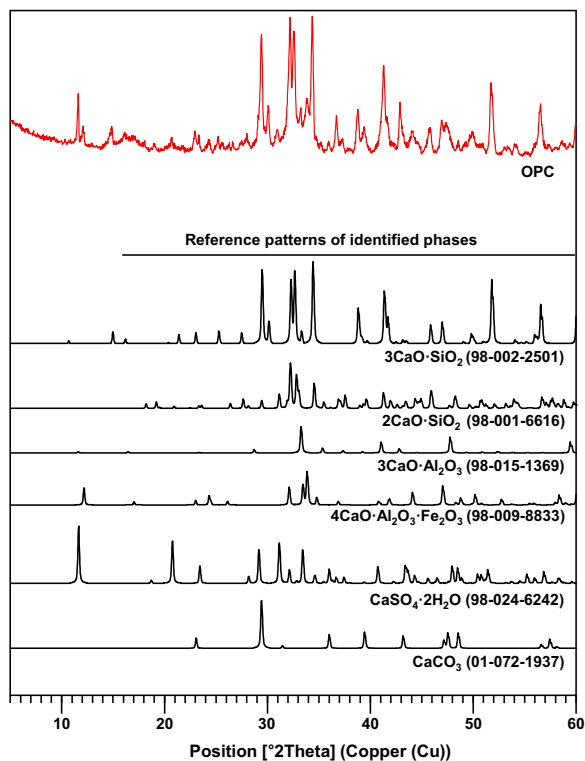

Fig. 2 Particle size distribution of raw ordinary Portland cement

wt%). Al$_2$O$_3$ and SO$_3$ contents mainly contribute to sulfate attack resistance performance by determining the amount of 3CaO·Al$_2$O$_3$ (C$_3$A) and gypsum (CaSO$_4$·2H$_2$O) production. The low contents of Al$_2$O$_3$ and SO$_3$ in Table 1 may imply high sulfate attack resistance due to the low proportion of C$_3$A and gypsum in the cement (Dyer 2014; Mehta and Monteiro, 2014).

Fig. 1 displays the powder XRD diffraction patterns for the raw OPC, which were measured by an X-ray diffractometer (D8 Advance; Bruker AXS, Fitchburg, WI, USA) with an incident beam of Cu-Kα radiation (λ = 1.5418 Å) for a 2θ scanning range of 5–60°. The XRD patterns were analyzed by using the X'pert High-Score Plus program (PANalytical, 2012) with the International Center for Diffraction Data (ICDD) PDF-2 database (Andersen et al., 2003; Wooster, 1930) and the Inorganic Crystal Structure Database (ICSD) (Allmann & Hinek, 2007). In the result of XRD, the raw OPC consisted of six types of cement compounds (3CaO·SiO$_2$, 2CaO·SiO$_2$, 3CaO·Al$_2$O$_3$, 4CaO·Al$_2$O$_3$·Fe$_2$O$_3$, CaSO$_4$·H$_2$O, and

CaCO$_3$). The cement contained mostly alite (3CaO·SiO$_2$), belite (2CaO·SiO$_2$), and a relatively low amount of aluminum-bearing cement compounds (3CaO·Al$_2$O$_3$ and 4CaO·Al$_2$O$_3$·Fe$_2$O$_3$), agreeing with the XRF result. Around five wt% of calcite (CaCO$_3$) was present as an admixture following the ASTM C150/C150M.

Particle size distributions of the raw OPC were measured with a laser diffraction particle size analyzer (HELOS (HI199) and RODOS; Sympatec, Clausthal-Zellerfeld, Lower Saxony, Germany). Fig. 2 presents the particle size distributions of the raw OPC, which had a median particle size of 11.61 μm.

The raw nano-aluminas were examined using the previous study's same methods and instruments (Maciver et al., 1963). In addition, a scanning electron microscope (SEM) was further employed to monitor the particle distribution because the nano-aluminas easily agglomerate with each other, which led to overestimating the particle size distribution measured by the laser diffraction particle analyzer (Yu et al., 2021). Briefly, the XRD patterns of α-alumina showed sharped crystalline peaks, while that of γ-alumina had an amorphous hump with five broad peaks, and the nano-aluminas' particle sizes were approximately 20 nm (Yu et al., 2021).

2.2 Sample Preparations and Test Methods
Table 2 presents the mixture proportions of paste samples in the study. Each nano-alumina added sample contains five wt% of each nano-alumina mixed with OPC.

In the study, no dispersing agent for nano-aluminas was used to eliminate the possibility of unwanted chemical reactions between nano-aluminas and chemical agents.

Yu *et al. Int J Concr Struct Mater*   (2023) 17:32

Page 4 of 11

Table 2 Mixture proportions of paste samples (wt%)

Sample labels	Binder				Water	w/b
	OPC	α-alumina	γ-alumina	Total		
OPC-0 (control)	100	0	0	100	40	0.4
OPC-A	95	5	0	100	40	0.4
OPC-G	95	0	5	100	40	0.4

OPC ordinary Portland cement, *w/b* water-to-binder weight ratio

The dry constituents were initially dry-mixed for 5 min in an enclosed chamber to improve dispersion of nano-alumina, and then water was added to obtain w/b = 0.4. Fresh paste samples were cast in three different molds (the size of 50 mm × 50 mm × 50 mm, 25 mm × 25 mm × 285 mm, and 40 mm × 40 mm × 160 mm) and cured at 35 °C and 99.9% relative humidity for one day. After 1 day of curing, the samples were demolded and immersed under Na_2SO_4 solution (352 mol of Na_2SO_4 per m^3) until tested. The Na_2SO_4 solution was renewed, as per ASTM C1012/C1012M, at one, two, three, four, eight, 13, 15, 16, and 24 weeks.

Compressive strength tests were carried out for each mixture proportion using triplicate samples with sizes of 50 mm × 50 mm × 50 mm after 1 day of curing and 28, 91, and 180 days of Na_2SO_4 exposure. After the mechanical test, the fragments of the fractured samples were ground with isopropanol for XRD and TG tests. In this study, the observation of ettringite is crucial to identify the cause of sulfate attack (Dyer 2014; Mehta and Monteiro, 2014). Since ettringite is easily deformed at a temperature above 40 °C, the process of hydration stoppage for each sample should be carefully treated (Winnefeld et al., 2016). Thus, the samples were immersed in isopropanol for one hour, filtered with diethyl ether as a second solvent exchange, and oven-dried at 40 °C for 10 min (Failed xxxx). Visual inspection was undertaken before compressive strength tests (one day of curing and 28, 91, and 180 days of Na_2SO_4 exposure).

Length change measurement was recorded over time as per ASTM C1012/C1012M at every Na_2SO_4 solution renewal. Before immersing the samples in the sulfate solution, the triplicate samples with 25 mm × 25 mm × 285 mm were measured as their initial length. The sample surface was wiped gently with a dry cloth on each designated measurement date, and then the length of the samples was quickly measured using a length comparator apparatus to avoid drying and shrinkage of the samples. The length change can be defined as follows:

$$\Delta L = \frac{L_x - L_i}{L_g} \times 100 \tag{1}$$

where ΔL = change in length at x age [%]; L_x = comparator reading of specimen at the age of x days—reference bar comparator reading at the age of x days; L_i = initial comparator reading of specimen—reference bar comparator reading, at the same time; and L_g = nominal gauge length, 250 mm.

The longitudinal dynamic elastic moduli of cement paste were measured according to ASTM C215-19 to compare the samples' decreasing rate of dynamic elastic moduli to ettringite and gypsum content, which could lead to internal expansion under sulfate exposure (Zhu et al., 2013). The bar samples with the size of 40 × 40 × 160 mm in Na_2SO_4 solution were wiped gently with a dry cloth, and then an accelerometer was installed at the sample end surface. The other end surface of the samples was impacted with a steel impactor five times to obtain reliable data. The data sampling rate was 50 kHz, and the dynamic Young's modulus of elasticity in pascals from the fundamental longitudinal frequency was calculated as follows:

$$Dynamic\ E = DM\left(n'\right)^2 \tag{2}$$

where: D = 4 (L/bt) $[m^{-1}]$; L = length of specimen [m]; b = dimension of prism cross-section perpendicular to t [m]; t = dimension of prism cross-section in the direction the prism is impacted [m]; M = mass of specimen [kg]; and n' = fundamental longitudinal frequency [Hz].

The XRD measurements were conducted with the ground samples to identify reaction products exposed to Na_2SO_4 solution using the same instrument and setup used for measuring raw materials. The same analysis software and databases in the raw material analysis were used to analyze the XRD patterns, but the reference pattern of C-S-H, the main reaction product in hydrated cement and semi-amorphous to X-ray, was obtained from 22-year-old β-2CaO·SiO$_2$ (β-C_2S) paste after deleting Ca(OH)$_2$ from the original pattern (Mohan & Taylor, 1981).

Yu *et al. Int J Concr Struct Mater* (2023) 17:32

Page 5 of 11

The TG measurements (SDT Q600; TA Instruments, New Castle, DE, USA) were undertaken. The temperature range for the test was 25–1000 °C with a heating rate of 10 °C/min in a nitrogen atmosphere. This study calculated portlandite content using the thermo-gravimetric method to compare the relationship between portlandite consumption and hydrates produced for each sample (Singh et al., 2015). The weight loss between 400 and 500 °C was considered as portlandite decomposition, and portlandite content in all samples was calculated from the TG curves using the following equation (Singh et al., 2015).

$$CH(\%) = WL\%(CH) \times \frac{MW(CH)}{MW(H)} \quad (3)$$

where: $CH(\%)$ = calculated portlandite content (%); $WL\%(CH)$ = the mass loss in percentage attributable to portlandite; $MW(CH)$ = molecular weights of portlandite; $MW(H)$ = molecular weight of water.

3 Results and Discussion

3.1 Compressive Strength

Fig. 3 shows the strength testing results for the paste samples. Before the Na_2SO_4 solution immersion, the γ-alumina added cement paste (OPC-G) displayed a slightly higher strength (by 2.0 MPa) compared to the control sample (OPC-0) at the same age. In contrast, the lowest compressive strength was found in the α-alumina added samples (OPC-A).

After Na_2SO_4 immersion, the compressive strength of all alumina added samples increased until 28 days; however, the strength started to decrease after 28 days of Na_2SO_4 immersion. In particular, OPC-G showed more rapid compressive strength degradation, although their greatest compressive strength among the test sets at 28 days of Na_2SO_4 exposure. The OPC-A and OPC-0
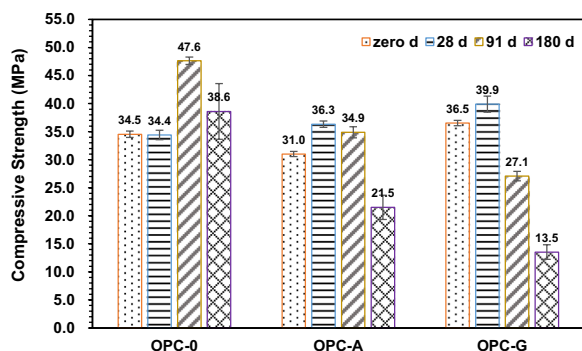
samples lost their compressive strength at 180 days of Na_2SO_4 exposure, but the strength reductions were not as severe as those of the OPC-G samples. After 180 days of Na_2SO_4 exposure, the compressive strength was found in the order of OPC-0 > OPC-A > OPC-G. The strength degradation mechanism of specimens is discussed in the following sections.

3.2 Visual Inspection of Samples

Fig. 4 shows the visual appearances of all samples before and after Na_2SO_4 exposure (i.e., after 28, 91, and 180 days of Na_2SO_4 immersion). The images display no difference among samples before Na_2SO_4 exposure. It should be noted that the sample strengths increased despite the presence of microcracks on the surfaces of OPC-A and OPC-G at 28 days of Na_2SO_4 exposure. From 28 days of Na_2SO_4 exposure, considerable cracks formed in OPC-A and OPC-G in the form of ring-shaped cracks. Notably, it was found that OPC-G was the most susceptible to Na_2SO_4 ingression by presenting severe disintegration. In contrast, the control samples (OPC-0) showed the least severe damage on all days of immersion, aligning with the compressive strength result.

3.3 Length Change of Immersed Samples

Fig. 5 shows the length change of the samples after being exposed to Na_2SO_4 solution. The length change was differed by the presence of nano-alumina in the cement pastes and the crystalline type of the added nano-alumina. All samples did not show a linear increase in length until 21 days of Na_2SO_4 exposure, but the lengths steadily increased after 21 days. The OPC-A displayed a similar trend to OPC-0 but a slightly greater length change over time. On the other hand, the OPC-G shrunk between 14 and 28 days of Na2SO4 exposure significantly, and then their vertical length increased drastically, particularly after 91 days. At 180 days of the Na_2SO_4 exposure, OPC-G showed the most significant length change, resulting in the complete destruction of two samples.

3.4 Dynamic Elastic Modulus

Fig. 6 shows the longitudinal dynamic modulus of elasticity of specimens before and after Na_2SO_4 exposure. Both OPC-A and OPC-G had lower dynamic moduli than OPC-0 during the entire experimental period. The dynamic elastic modulus of all samples increased gradually, but OPC-A and OPC-G showed a declination after reaching the peak dynamic modulus within 91 days of Na_2SO_4 exposure. The decrease in the dynamic modulus of cementitious binders exposed to sulfate could be linked to length expansion (Chen et al., 2020; Rocco et al., 2004; Zhu et al., 2013). A
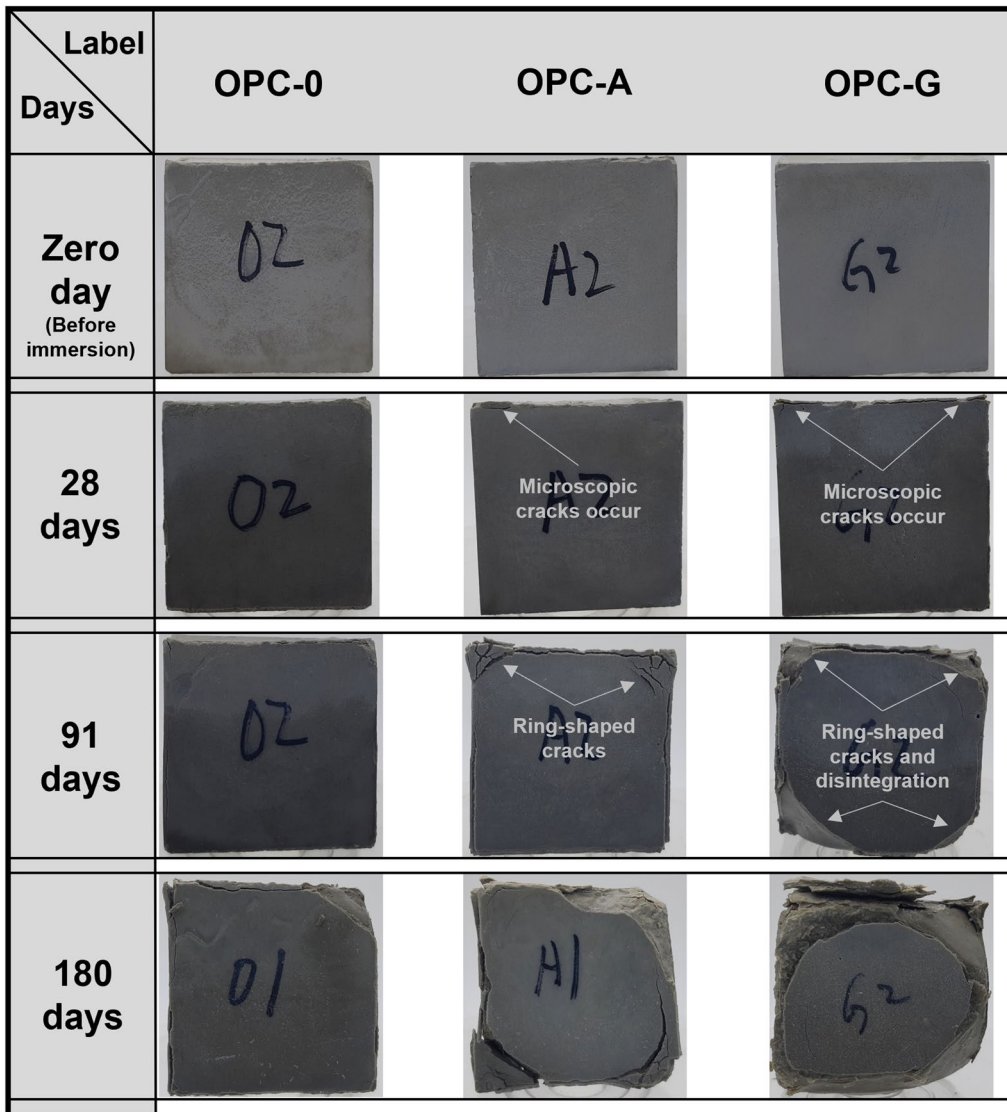
Fig. 3 Compressive strengths of hardened paste samples before Na_2SO_4 immersion (zero d) and after Na_2SO_4 exposure (28, 91, and 180 d). Error bars are the standard deviations of the measured strengths for triplicate samples

Yu *et al. Int J Concr Struct Mater* (2023) 17:32

Page 6 of 11

Label\Days	OPC-0	OPC-A	OPC-G
Zero day (Before immersion)			
28 days		Microscopic cracks occur	Microscopic cracks occur
91 days		Ring-shaped cracks	Ring-shaped cracks and disintegration
180 days			

Fig. 4 The visual appearances of specimens at zero (before immersion), 28, 91, and 180 days in Na_2SO_4 solution
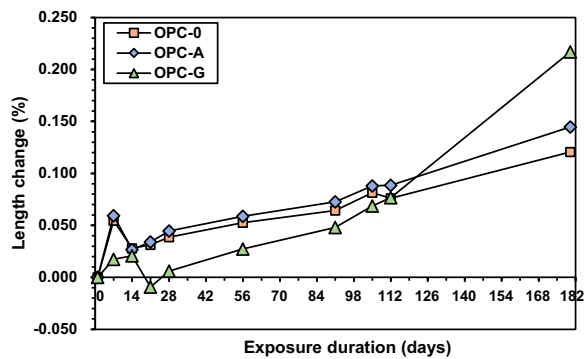
Fig. 5 The length change of specimens after Na_2SO_4 exposure
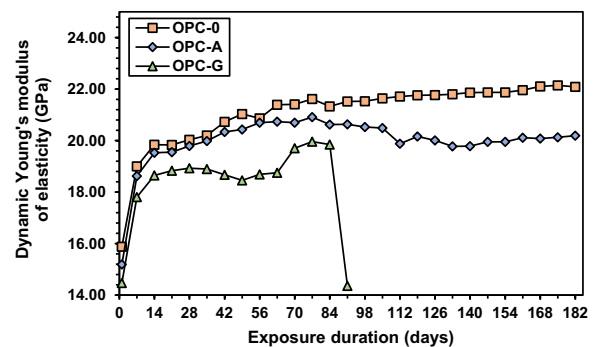
Fig. 6 Dynamic elastic modulus curves of the specimens after Na_2SO_4 exposure

Yu et al. Int J Concr Struct Mater (2023) 17:32

Page 7 of 11

significant increase in length of OPC-A and OPC-G was found after 91 days of Na_2SO_4 exposure. Notably, a sharp increase point in length change and a decrease in dynamic modulus of OPC-G were matched at a similar experimental period. Thus, the rapid length expansion of OPC-G likely affected their dynamic modulus reduction (Chen et al., 2020; Rocco et al., 2004; Zhu et al., 2013). The dynamic modulus of OPC-A continuously decreased at a slower pace than OPC-G, which aligns with the length change result. This study found that the nano-alumina inclusion in cement pastes adversely increased in length under Na_2SO_4 exposure, leading to worsened mechanical properties, such as compressive strength and dynamic modulus. In chemical regard, the declination of dynamic elastic modulus is closely related to the destructive effect of the internal stress due to the expansion products such as ettringite and gypsum (Zhu et al., 2013), which will be discussed in XRD and TG, and DTG results.

3.5 XRD

Fig. 7 shows the XRD patterns of all samples before (zero day) and after Na_2SO_4 exposure (28, 91, and 180 days) with the reference patterns from the ICDD and the ICSD
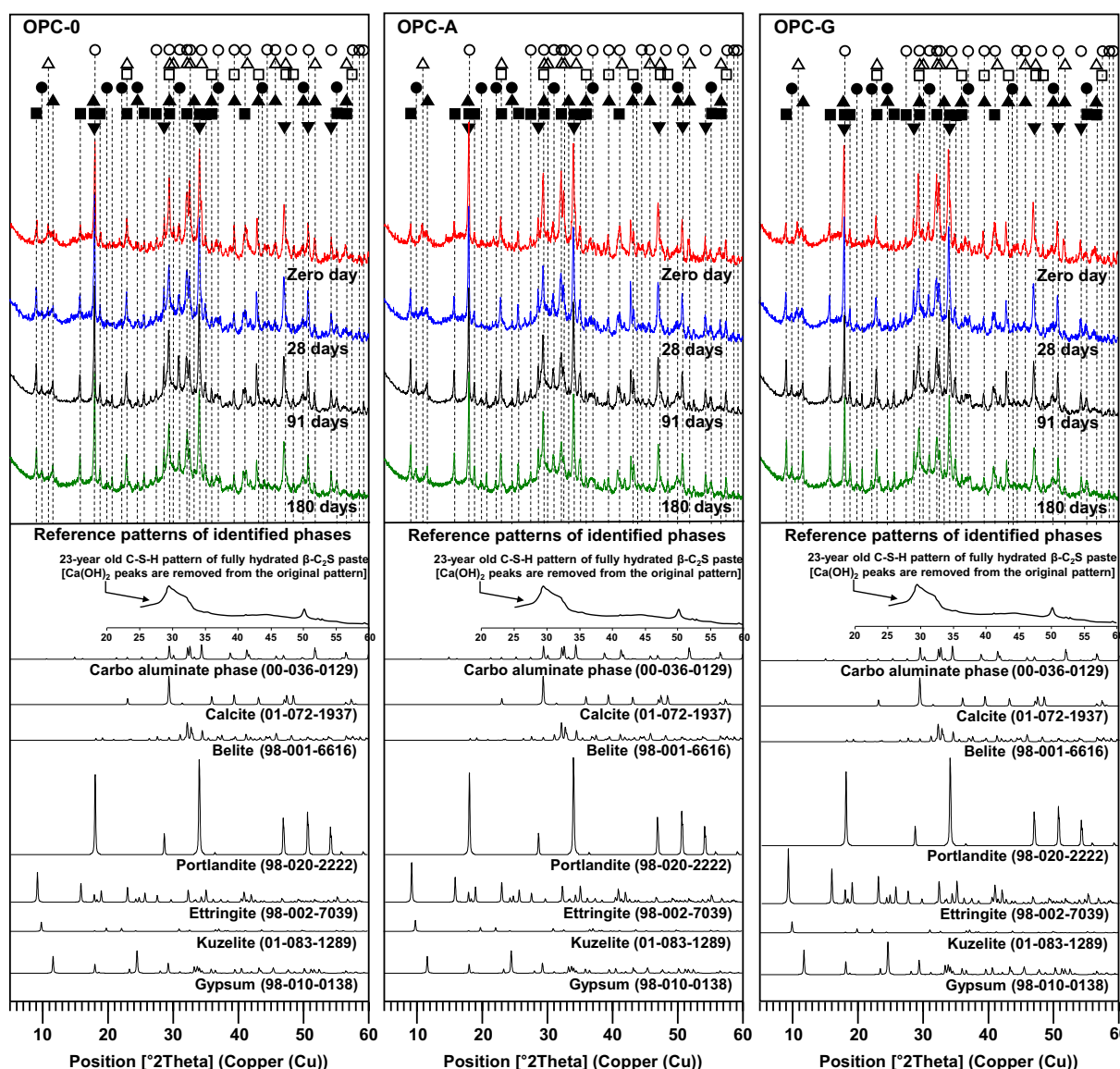

Fig. 7 The XRD patterns of all samples before Na_2SO_4 exposure (zero day exposure) and after Na_2SO_4 exposure (28, 91, and 180 days of Na_2SO_4 exposure) with the reference patterns from the ICDD and the ICSD database. ■ Ettringite, ▲ Gypsum, ● Kuzelite, ▼ Portlandite, □ Calcite, △ Carbo-aluminate phase, ○ Belite

Yu et al. Int J Concr Struct Mater   (2023) 17:32

Page 8 of 11

database to identify the phases. The peak intensity scales of all reference patterns in the result were altered to resemble the identified mineral phases in the measured XRD patterns.

The reaction products identified in the study were carbo-aluminate phase ($4CaO \cdot Al_2O_3 \cdot CO_2 \cdot 11H_2O$), ettringite [$Ca_6Al(SO_4)_3(OH)_{12} \cdot 26H_2O$], portlandite [$Ca(OH)_2$], kuzelite [$Ca_4 \cdot Al_2 \cdot 4OH \cdot 12.8SO_4 \cdot 6H_2O$], and gypsum ($CaSO_4 \cdot 2H_2O$). The peaks of the carbo-aluminate phase were observed in all samples before Na_2SO_4 exposure (zero day) but decreased after Na_2SO_4 exposure because of the transformation of the carbo-aluminate phase into ettringite or kuzelite (Feng et al., 2015; Irassar, 2009; Irassar et al., 2003).

Before sulfate exposure, all samples had similar peak intensities of ettringite, but a higher ettringite was observed in OPC-A and OPC-G. Higher ettringite formation of nano-alumina incorporated samples after 28 days of Na_2SO_4 could exert internal stress due to its expansive properties (Zhu et al., 2013), resulting in volume expansion and a decline in dynamic elastic modulus and compressive strength in the study. Additionally, the amount of ettringite formation differed in the crystallinity degree of nano-aluminas due to different dissolution rates of nano-aluminas (Shao et al., 2019; Yu et al., 2021; Zhou et al., 2019). Nano-alumina reacted with portlandite, producing AH_3 gel in the following Eq. (4) (Zhou et al., 2019). Since AH_3 gel is amorphous and easily reacts with sulfur, forming ettringite, direct detection of AH_3 gel was not possible in the study (Yu et al., 2021). However, XRD results showed that OPC-G had relatively lower peak intensities of portlandite than OPC-A, indicating a high amount of AH_3 gel formation, which might react with intruding sulfate after 28 days of Na_2SO_4 exposure.

A significant increase in the peak intensities of gypsum was observed in the OPC-G at 180 days of Na_2SO_4 exposure due to the alumina dissolution process (Zhou et al., 2019). In Eq. (4), alumina transformation produces free Ca^{2+} ions, which normally react with gypsum, forming ettringite (Zhou et al., 2019).

$$Al_2O_3 \cdot xH_2O_{(s)} + 2CaOH^-_{(aq)}$$
$$\leftrightarrow 2Al(OH)^-_{4(aq)} + (x-3)H_2O + 2Ca^{2+}_{(aq)} \quad (4)$$
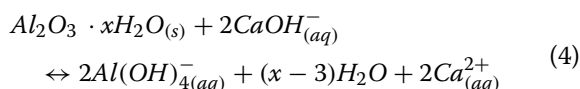
In the study, these free calcium ions likely reacted with AH_3 gel, gypsum, and $CaCO_3$ present in OPC, producing ettringite, kuzelite, and carbo-aluminate phase at the early days of Na_2SO_4 exposure. Additionally, during the experiment, the Na_2SO_4 solution intrusion was accelerated due to the increasing surface disintegration of OPC-G, which provided a high sulfate source for gypsum formation. Thus, the alumina dissolution

released the free calcium ions, and a high amount of sulfate from Na_2SO_4 might produce additional gypsum at 180 days of Na_2SO_4 exposure (Zhou et al., 2019).

In the sulfate attack, gypsum formation causes internal expansion (approximately 120% expansion) in the following chemical reactions, leading to cracking (Dyer 2014; Mehta and Monteiro, 2014).

$$Ca^{2+}_{(aq)} + SO^{2-}_{4(aq)} + 2H_2O_{(l)} \rightarrow CaSO_4 \cdot 2H_2O \quad (5)$$
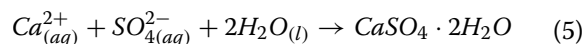
Thus, the excessive ettringite and gypsum formation in this study further contributed to the severe cracking in OPC-G samples. Additionally, the time at which OPC-G showed the drastic length change coincided with a period of rapid increase in the gypsum formation, demonstrating that a large gypsum formation was likely responsible for the further increase in sample length.

3.6 TG and DTG

Fig. 8 presents the TG and DTG test results before (zero day) and after Na_2SO_4 exposure for the total weight loss at a temperature range between 25 and 1000 °C.

In the TG result, the total weight losses of all samples gradually increased with increasing days of the Na_2SO_4 exposure. Overall, OPC-G showed the greatest weight loss in the temperature region up to 200 °C during all experimental periods. In the case of OPC-A, the weight loss was similar to that of the control samples up to 28 days of Na_2SO_4 exposure, but the weight loss became higher than that of the control sample after 28 days of Na_2SO_4 exposure. In the TG results above 200 °C, all samples showed two weight loss regions near 380–440 °C and 620–720 °C in all exposure periods. The total weight loss of all samples up to 1000 °C increased until 91 days of Na_2SO_4 exposure and slightly decreased on 180 days of Na_2SO_4 exposure.

The DTG results display reaction products identified with reference to earlier studies (Failed, 2002; Jeong et al., 2016; Park et al., 2016; Song et al., 2018; Yu et al., 2021). The chemical compounds identified in the DTG results included C-S-H, ettringite, AFm (Al_2O_3–Fe_2O_3-mono) phases (carbo-aluminate phases and kuzelite), gypsum, portlandite, and residual calcite consistent with the XRD results. In general, two distinct DTG peaks in all samples were observed in the pre-200 °C region. The first DTG peak (80–100 °C) indicated dehydration of ettringite and C-S-H (Failed, 2002; Jeong et al., 2016; Park et al., 2016; Song et al., 2018). Before 28 days of Na_2SO_4 exposure, all samples displayed similar intensities of the first DTG peaks. However, the first DTG peak in OPC-G increased drastically after 28 days of Na_2SO_4 exposure, compared to other samples (OPC-0 and OPC-A), due to the increased quantities of ettringite formation.
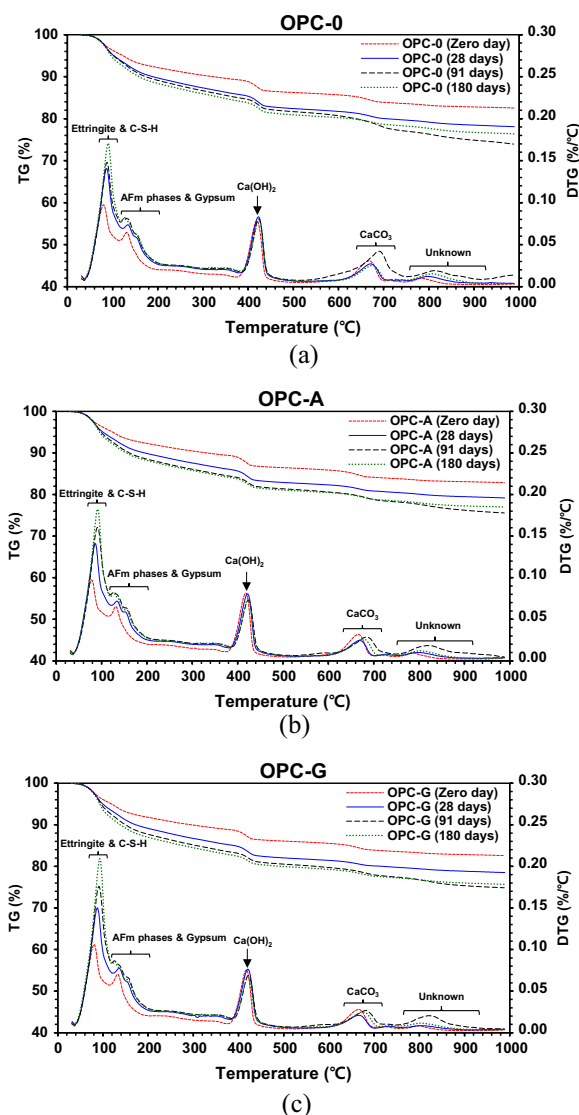
Yu et al. Int J Concr Struct Mater   (2023) 17:32

Page 9 of 11

Fig. 8 TG and DTG results of the hardened samples before Na_2SO_4 exposure (zero day exposure) and after Na_2SO_4 exposure (28, 91, and 180 days of Na_2SO_4 exposure): **a** TG and DTG result of the control samples (OPC-0), **b** TG and DTG result of the α-alumina added samples (OPC-A), and **c** TG and DTG result of the γ-alumina added samples (OPC-G)

Table 3 Portlandite content in Na_2SO_4 solution exposed cement paste samples (%)

Sample labels	Na_2SO_4 solution exposure			
	Zero-day	28 days	91 days	180 days
OPC	10.61	12.05	11.84	11.72
OPC-A	10.24	11.35	11.10	10.94
OPC-G	9.62	11.19	10.57	10.04

Irassar, 2009; Irassar et al., 2003). OPC-A and OPC-G showed greater DTG peaks than OPC-0 in that temperature range. Mainly, the largest DTG peaks could be found in OPC-G, meaning that γ-alumina addition increased the formation of carbo-aluminate phases, kuzelite, and gypsum matched with the XRD results (Shao et al., 2019; Yu et al., 2021; Zhou et al., 2019).

The DTG peaks near 450 °C indicate the dehydration of portlandite (Singh et al., 2015; Song et al., 2018). Table 3. presents calculated portlandite content in all paste samples at different days of Na_2SO_4 solution exposure. In the table, the portlandite in all samples started to decrease after 28 days of Na_2SO_4 exposure, and its decrease occurred with an increase in hydrates such as ettringite and AFm phase. Nano-alumina added sample showed lower portlandite content than the control sample under Na_2SO_4 solution exposure due to (1) AH_3 gel formation and (2) an increase in Al-bearing hydrates formation such as ettringite or kuzelite (Shao et al., 2019; Yu et al., 2021; Zhou et al., 2019). The DTG peak of AH_3 gel from γ-alumina could find near 250 °C in a low sulfur environment (Yu et al., 2021), but OPC-G showed no distinct DTG peak near 250 °C during all Na_2SO_4 exposure periods, probably due to unexpected extra ettringite formation with intruding Na_2SO_4 solution. Lower portlandite content and higher DTG peak for ettringite in OPC-A than in the control sample support possible AH_3 gel transformation of α-phase nano-alumina under Na_2SO_4 exposure, which also generated ettringite more. The additional ettringite formation in OPC-G and OPC-A after 28 days of Na_2SO_4 exposure could not act as pore densification but rather cause volume expansion and crack propagation shown in the aforementioned results.

The DTG peak near 650 °C represented the calcite decarbonization. Before Na_2SO_4 exposure and in the early age of Na_2SO_4 exposure (Up to 28 days), the calcite DTG peak decreased slightly, possibly because of the formation of carbo-aluminate phases. A high calcite consumption in OPC-G was well-matched with the high

The other DTG peaks (120–180 °C) were associated with carbo-aluminate phases, kuzelite, and gypsum (Jeong et al., 2016; Shao et al., 2019; Yu et al., 2021). These DTG peaks split into multiple peaks with increasing Na_2SO_4 exposure time because of (1) the transformation of carbo-aluminate into ettringite and kuzelite and (2) the formation of gypsum and kuzelite (Feng et al., 2015;

Yu *et al. Int J Concr Struct Mater*   (2023) 17:32

Page 10 of 11

amount of carbo-aluminate phases observed in the XRD result.

An unexpected increase in the calcite could be found in the DTG result of the control samples at 91 days of Na_2SO_4 exposure because of carbon reaction during the experimental procedure. However, the DTG results still implied the same conclusion: the addition of nano-alumina accelerated the formation of ettringite and gypsum after Na_2SO_4 exposure, resulting in severe volume expansion and crack propagation. In addition, the high dissolution rate of γ-alumina accelerated the sulfate attack degradation.

4 Conclusions

The main objective of this study is to investigate the impact of supplementary hydration products from nano-alumina incorporation in ordinary Portland cement paste under sulfate attack. This may cause two opposite phenomena: (1) impediment of sulfate ingress through pore refinement (beneficial effect); (2) internal stress induction from the volume expansion of excessive hydration product formation (adverse effect). Both nano-alumina incorporated samples (OPC-A and OPC-G) experienced rapid compressive strength loss, initiating from 28 days of Na_2SO_4 solution exposure, with increasing length expansion. At the same time, the control sample (OPC-0) showed continuous compressive strength development up to 91 days of Na_2SO_4 exposure. Severe ring-shaped cracks were observed in all the nano-alumina incorporated samples, but OPC-G remarkably showed a further disintegration under Na_2SO_4 exposure. On top of that, a rapid descending zone of modulus was found in the nano-alumina incorporated samples referring to the expansion products within the cement paste instigating internal stress. To clarify the strength loss mechanism, XRD and TG/DTG were employed. The results of OPC-A and OPC-G showed a lower portlandite content and a higher amount of ettringite than the OPC-0. This could be interpreted as the chemical transformation of nano-alumina into AH_3 gel by consuming portlandite, causing extra ettringite formation during Na_2SO_4 exposure. The higher portlandite consumption rate in the OPC-G sample could imply a greater AH_3 gel formation than OPC-A, and this hydrate could react with intruding sulfate, resulting in undesirable expansion products formation such as ettringite. This could be seen as a primary factor in the strength loss, length expansion and descending zone of modulus. The aforementioned observations conclude that the pore refinement action of γ-alumina would not effectively prevent sulfate permeation but rather increases the amount of expansive reactive hydrates such as ettringite or gypsum through AH_3 gel formation and

deteriorates the sulfate resistance. Thus, such internal expansion stress development during sulfate exposure shall be considered during material design for nano-alumina addition in concrete. A stoichiometric dosage of sulfuric source, like gypsum, can be considered as a potential mitigation towards such adverse effects as it is believed to maximize the early hydration of nano-alumina with supplementary gypsum content and minimize the late transformation into AH_3 gel which can be studied in the future.

Authors' information
Juan Yu is a Graduate student in Department of Urban and Environmental Engineering at Ulsan National Institute of Sciences and Technology (UNIST), Ulsan, Korea.
Sungwon Sim is a Postdoctoral Researcher in Department of Urban and Environmental Engineering at Ulsan National Institute of Sciences and Technology (UNIST), Ulsan, Korea.
Haemin Song is a Postdoctoral Researcher in Department of Urban and Environmental Engineering at Ulsan National Institute of Sciences and Technology (UNIST), Ulsan, Korea.
Dohoon Kim is a Graduate student in Department of Urban and Environmental Engineering at Ulsan National Institute of Sciences and Technology (UNIST), Ulsan, Korea.
Kyungcheol Jang is a Graduate student in Department of Urban and Environmental Engineering at Ulsan National Institute of Sciences and Technology (UNIST), Ulsan, Korea.
Dongho Jeon is a Postdoctoral Researcher in Department of Civil and Environmental Engineering at Seoul National University, Seoul, Korea, and was in Department of Urban and Environmental Engineering at Ulsan National Institute of Sciences and Technology (UNIST), Ulsan, Korea.
Seung Cho is a Postdoctoral Researcher in Department of Urban and Environmental Engineering at Ulsan National Institute of Sciences and Technology (UNIST), Ulsan, Korea, and was Division for Structural Engineering and Civil Engineering Informatics, Department of Civil Engineering, Stellenbosch University, Stellenbosch 7600, South Africa
Ja Eun Oh is a Full Professor in Department of Urban and Environmental Engineering at Ulsan National Institute of Sciences and Technology (UNIST), Ulsan, Korea.

Availability of data and materials
Not applicable.

Declarations

Ethics approval and consent to participate
Not applicable.

Yu *et al. Int J Concr Struct Mater*   (2023) 17:32

Page 11 of 11

References

Acikgoz, M., Harrell, J., & Pavanello, M. (2018). Seeking a structure–function relationship for γ-Al2O3 surfaces. *The Journal of Physical Chemistry C, 122*(44), 25314–25330.

Allmann, R., & Hinek, R. (2007). The introduction of structure types into the inorganic crystal structure database ICSD. *Acta Crystallographica Section a: Foundations of Crystallography, 63*(5), 412–417.

Andersen, M. D., Jakobsen, H. J., & Skibsted, J. (2003). Incorporation of aluminum in the calcium silicate hydrate (C— S— H) of hydrated portland cements: a high-field 27Al and 29Si MAS NMR investigation. *Inorganic Chemistry, 42*(7), 2280–2287.

Antao, S. M., Duane, M. J., & Hassan, I. (2002). DTA, TG, and XRD studies of sturmanite and ettringite. *The Canadian Mineralogist, 40*(5), 1403–1409.

Chen, J., Liang, C., Li, B., Wang, E., Li, G., & Hou, X. (2018). The effect of nano-γAl2O3 additive on early hydration of calcium aluminate cement. *Construction and Building Materials, 158*, 755–760.

Chen, Y., Liu, P., & Yu, Z. (2020). Study on degradation of macro performances and micro structure of concrete attacked by sulfate under artificial simulated environment. *Construction and Building Materials, 260*, 119951.

Dyer, T. (2014). *Concrete durability*. Boca Raton: Crc Press.

Farzadnia, N., Ali, A. A. A., & Demirboga, R. (2013). Characterization of high strength mortars with nano alumina at elevated temperatures. *Cement and Concrete Research, 54*, 43–54.

Feng, P., Garboczi, E. J., Miao, C., & Bullard, J. W. (2015). Microstructural origins of cement paste degradation by external sulfate attack. *Construction and Building Materials, 96*, 391–403.

Gopalakrishnan, R., & Jeyalakshmi, R. (2020). The effects on durability and mechanical properties of multiple nano and micro additive OPC mortar exposed to combined chloride and sulfate attack. *Materials Science in Semiconductor Processing, 106*, 104772.

Huang, Q., Zhao, L., Zhao, C., Liu, D., & Wang, C. (2020). Microstructure change of nanosilica-cement composites partially exposed to sulfate attack. *International Journal of Concrete Structures and Materials, 14*(1), 1–11.

Irassar, E. (2009). Sulfate attack on cementitious materials containing limestone filler—A review. *Cement and Concrete Research, 39*(3), 241–254.

Irassar, E., Bonavetti, V., & Gonzalez, M. (2003). Microstructural study of sulfate attack on ordinary and limestone portland cements at ambient temperature. *Cement and Concrete Research, 33*(1), 31–41.

Jeong, Y., Park, H., Jun, Y., Jeong, J. H., & Oh, J. E. (2016). Influence of slag characteristics on strength development and reaction products in a CaO-activated slag system. *Cement and Concrete Composites, 72*, 155–167.

Li, W., Li, X., Chen, S. J., Long, G., Liu, Y. M., & Duan, W. H. (2017). Effects of nanoalumina and graphene oxide on early-age hydration and mechanical properties of cement paste. *Journal of Materials in Civil Engineering, 29*(9), 04017087.

Maagi, M. T., Lupyana, S. D., & Gu, J. (2019). Effect of nano-SiO2, nano-TiO2 and nano-Al2O3 addition on fluid loss in oil-well cement slurry. *International Journal of Concrete Structures and Materials, 13*(1), 1–6.

Maciver, D. S., Tobin, H. H., & Barth, R. (1963). Catalytic aluminas I. Surface chemistry of eta and gamma alumina. *J Catal, 2*(6), 485–497.

Mehta, P. K., Monteiro, P. J. M. (2014). Concrete: microstructure, properties, and materials. McGraw-Hill Education.

Mohan, K., & Taylor, H. (1981). Analytical electron microscopy of cement pastes: IV, β-dicalcium silicate pastes. *Journal of the American Ceramic Society, 64*(12), 717–719.

Mohseni, E., Kazemi, M. J., Koushkbaghi, M., Zehtab, B., & Behforouz, B. (2019). Evaluation of mechanical and durability properties of fiber-reinforced lightweight geopolymer composites based on rice husk ash and nano-alumina. *Construction and Building Materials, 209*, 532–540.

Mukhopadhyay, A. K. (2011). Next-generation nano-based concrete construction products: a review. In Kasthurirangan Gopalakrishnan, Bjorn Birgisson, Peter Taylor, & Nii O. Attoh-Okine (Eds.), *Nanotechnology in civil infrastructure* (pp. 207–223). Berlin: Springer Berlin Heidelberg.

Newsome, J., Heiser, H., Russell, A., & Stumpf, H. (1960). *Alumina properties. technical paper no. 10 second revision*. New Kensington: Aluminum Co. of America. Alcoa Research Labs.

PANalytical B. 2012 Pert HighScore Plus software, version 3.0 e, Almelo: Netherlands

Park, H., Jeong, Y., Jun, Y., Jeong, J.-H., & Oh, J. E. (2016). Strength enhancement and pore-size refinement in clinker-free CaO-activated GGBFS systems through substitution with gypsum. *Cement and Concrete Composites, 68*, 57–65.

Qudoos, A., Jakhrani, S. H., Kim, H. G., & Ryou, J.-S. (2019). Influence of nano-silica on the leaching attack upon photocatalytic cement mortars. *International Journal of Concrete Structures and Materials, 13*(1), 1–12.

Rocco C, Giandrasso F, Bergol L, Di Pace G, Planas J. Fracture properties of concrete exposure to delayed ettringite formation, proceedings of the 5th Int. Conference on fracture Mechanics of Concrete an Concrete Structures, 2004, pp. 623–630.

Scrivener, K., Snellings, R., & Lothenbach, B. (2018). *A practical guide to microstructural analysis of cementitious materials*. Boca Raton: Crc Press.

Shahrajabian, F., & Behfarnia, K. (2018). The effects of nano particles on freeze and thaw resistance of alkali-activated slag concrete. *Construction and Building Materials, 176*, 172–178.

Shao, Q., Zheng, K., Zhou, X., Zhou, J., & Zeng, X. (2019). Enhancement of nano-alumina on long-term strength of portland cement and the relation to its influences on compositional and microstructural aspects. *Cement and Concrete Composites, 98*, 39–48.

Singh, L. P., Goel, A., Bhattachharyya, S. K., Ahalawat, S., Sharma, U., & Mishra, G. (2015). Effect of morphology and dispersibility of silica nanoparticles on the mechanical behaviour of cement mortar. *International Journal of Concrete Structures and Materials, 9*(2), 207–217.

Song, H., Jeong, Y., Bae, S., Jun, Y., Yoon, S., & Oh, J. E. (2018). A study of thermal decomposition of phases in cementitious systems using HT-XRD and TG. *Construction and Building Materials, 169*, 648–661.

Winnefeld, F., Schöler, A., & Lothenbach, B. (2016). *Sample preparation a practical guide to microstructural analysis of cementitious materials*. Boca Raton: Crc Press.

Wooster, N. (1930). International center for diffraction data. *Kristall, 74*, 363.

Xie, J., Li, J., Lu, Z., Li, Z., Fang, C., Huang, L., & Li, L. (2019a). Combination effects of rubber and silica fume on the fracture behaviour of steel-fibre recycled aggregate concrete. *Construction and Building Materials, 203*, 164–173.

Xie, J., Zhao, J., Wang, J., Wang, C., Huang, P., & Fang, C. (2019b). Sulfate resistance of recycled aggregate concrete with GGBS and fly ash-based geopolymer. *Materials, 12*(8), 1247.

Yu, J., Song, H., Jeon, D., Sim, S., Kim, D., Lee, H., Yoon, S., Yum, W. S., & Oh, J. E. (2021). Influence of the degree of crystallinity of added nano-alumina on strength and reaction products of the CaO-activated GGBFS system. *Construction and Building Materials, 296*, 123647.

Zhan, B. J., Xuan, D. X., & Poon, C. S. (2019). The effect of nanoalumina on early hydration and mechanical properties of cement pastes. *Construction and Building Materials, 202*, 169–176.

Zhou, J., Zheng, K., Liu, Z., & He, F. (2019). Chemical effect of nano-alumina on early-age hydration of portland cement. *Cement and Concrete Research, 116*, 159–167.

Zhu, J., Cao, Y.-H., & Chen, J.-Y. (2013). Study on the evolution of dynamic mechanics properties of cement mortar under sulfate attack. *Construction and Building Materials, 43*, 286–292.

Publisher's Note

Springer Nature remains neutral with regard to jurisdictional claims in published maps and institutional affiliations.